Physics of Fluids

Wavelet analysis of coherent vorticity near the turbulent/non-turbulent interface in a turbulent planar jet

Cite as: Phys. Fluids **26**, 095105 (2014); https://doi.org/10.1063/1.4896298
Submitted: 20 June 2014 • Accepted: 06 September 2014 • Published Online: 26 September 2014

T. Watanabe, Y. Sakai, K. Nagata, et al.

AIP Publishing

PHYSICS OF FLUIDS **26**, 095105 (2014)

Wavelet analysis of coherent vorticity near the turbulent/non-turbulent interface in a turbulent planar jet

T. Watanabe,[1,a)] Y. Sakai,[1] K. Nagata,[1] Y. Ito,[1] and T. Hayase[2]
[1]*Department of Mechanical Science and Engineering, Nagoya University, Nagoya, Japan*
[2]*Institute of Fluid Science, Tohoku University, Sendai, Japan*

(Received 20 June 2014; accepted 6 September 2014; published online 26 September 2014)

Coherent vorticity near the turbulent/non-turbulent (T/NT) interface is investigated by using direct numerical simulation of a planar jet. The coherent vorticity extraction (CVE) method based on the orthogonal wavelet decomposition of vorticity is applied to the planar jet for extracting the coherent vorticity. We analyze the conditional statistics conditioned on the distance from the T/NT interface. The coherent vorticity is reconstructed from small number of wavelet coefficients. Nevertheless, the coherent vorticity contains most of enstrophy in the planar jet. Furthermore, the characteristics of the vorticity field are well captured even near the T/NT interface by the coherent vorticity. The coherent velocity obtained by the Biot–Savart relation shows that the large-scale motions, such as induced flow and engulfing motion in the non-turbulent region, are also well represented by the coherent field. The enstrophy transport equation is decomposed into coherent and incoherent parts by the CVE for investigating the role of the coherent vorticity in the enstrophy transport mechanism. The conditional average of the enstrophy transport equation shows that the enstrophy production and dissipation associated with the incoherent vorticity are small compared with the coherent contributions. The enstrophy diffusion near the T/NT interface, which causes the local entrainment of non-turbulent fluids, arises from the coherent vorticity. Thus, most of the enstrophy transport mechanism near the T/NT interface is well captured by the coherent vorticity extracted by the CVE method. © *2014 AIP Publishing LLC*. [http://dx.doi.org/10.1063/1.4896298]

I. INTRODUCTION

Interfaces which divide flow fields into turbulent and non-turbulent regions can be observed in environmental and industrial flows. These interfaces are called turbulent/non-turbulent (T/NT) interface,[1] and appear in free shear flows, such as wakes, jets, and mixing layers. The free shear flows develop by converting the non-turbulent fluids near the T/NT interface into the turbulent fluids. Therefore, the T/NT interface plays an important role in the entrainment process, which largely affects heat and mass transfers in free shear flows. Understanding the characteristics of the T/NT interface is desired for controlling the entrainment rate and the heat and mass transfers in engineering equipments. The T/NT interface consists of turbulent sublayer[1] and viscous superlayer.[2] In the viscous superlayer, vorticity is transported by the viscous effect from turbulent regions, whereas the inviscid processes, such as vortex stretching and compression, are important in the turbulent sublayer.[3]

Westerweel *et al.* experimentally investigated the T/NT interface in a round jet, and revealed that the entrainment process is dominated by small-scale eddies near the T/NT interface.[4–6] The entrainment process has been investigated by analyzing the enstrophy transport equation. Holzner *et al.* conducted experiments on a turbulent front generated by an oscillating-grid by using particle

---

[a)] Research Fellow of the Japan Society for the Promotion of Science. watanabe.tomoaki@c.nagoya-u.jp tracking velocimetry,[7,8] and showed that the viscous process plays an important role in the T/NT interface propagation, which results in the entrainment of the non-turbulent fluids.[9] Direct numerical simulations (DNSs) of a temporally developing jet[10] were used for analyzing the enstrophy transport near the T/NT interface by Taveira *et al.*[11] They showed that the enstrophy growth in the non-turbulent region near the T/NT interface is caused by the viscous diffusion, whereas the enstrophy production dominates its generation inside the turbulent region. The vorticity diffusion near the interface caused by small-scale eddy motions is referred to as "nibbling." Thus, the previous studies have demonstrated the importance of the small-scale eddies in the local entrainment process because these eddies cause the enstrophy diffusion. However, the large-scale motions of non-turbulent fluids are also responsible for the total entrainment process.[12] The vortical structure near the T/NT interface was investigated by using DNS of the temporally developing jet by da Silva *et al.*[13,14] In their analysis, the intense vorticity structures are detected by thresholding vorticity magnitude, and the large vorticity structures are detected by low pressure isosurfaces. These studies showed that the thickness of the T/NT interface is almost equal to the radius of the large vorticity structures near the interface, and the intense vorticity structures near the T/NT interface are well modeled by the Burgers vortex.

Investigating vortical structures requires the extraction of specific vorticity from the total vorticity field. Farge *et al.* proposed the method to extract the coherent structure using the wavelet analysis.[15,16] This method splits the vorticity into the coherent and incoherent parts by using the orthogonal wavelet decomposition of the vorticity, and is called coherent vorticity extraction[17] (CVE). The CVE method is related to a denoising of signals in wavelet space. The CVE method has been applied to homogeneous isotropic turbulence.[16,18–20] Curvelet and total variation filtering methods, which decompose flow fields into coherent and incoherent parts, have also been applied to homogeneous isotropic turbulence to extract the coherent structure.[21,22] Low-pass Fourier filtering can also be used for the data compression of turbulent flows by discarding a small-scale part. When the Fourier filtering is applied at the compression rate similar to the CVE, the discarded part by the Fourier filtering shows spatial structures, which can be considered as the coherent part and important in turbulent flows.[25] In contrast, the discarded part by the CVE is structureless and uncorrelated in space.[25] These previous studies showed that the CVE based on the wavelet decomposition can more efficiently extract the coherent structures than the Fourier filtering. The CVE using the wavelet analysis has been demonstrated mainly for homogeneous isotropic turbulence. The CVE method was also applied to sheared and rotating turbulence,[23] mixing layers,[24,25] and boundary layers,[26] and succeeded in extracting the coherent structure. However, applications of the CVE method to inhomogeneous and anisotropic turbulence are limited. The CVE method is used in the coherent vorticity simulation (CVS), in which the evolution of the coherent vorticity is solved whereas the influence of the incoherent vorticity is modeled.[15,17] The CVS has been applied to turbulent mixing layers.[25,27] Because the CVE method extracts the coherent structure more efficiently than the Fourier filtering, the CVS has advantages over the large eddy simulation, in which the large-scale structure is extracted by the low-pass filtering such as the Fourier filter. Therefore, the further development of the CVS is desired for predicting turbulent flows.

In this work, the CVE method is applied to DNS results of a turbulent planar jet. We extract the coherent structure in the planar jet, and investigate the coherent vorticity near the T/NT interface. The purposes of this work are to extract the coherent vorticities in a turbulent jet and to investigate them near the T/NT interface. It has been shown that the small-scale eddies near the interface play an important role in the entrainment process. The characteristics of the vortical structure, such as the radius, circulation, and tangential velocity, were investigated near the T/NT interface.[14] However, the role of the vortical structure in the entrainment process still remains unclear. The entrainment of non-turbulent fluids is caused by the transport of vorticity near the interface. The CVE method enables us to directly investigate the contribution of the coherent vorticity to the enstrophy transport because the velocity fields corresponding to the coherent and incoherent vorticities can be obtained by using the Biot–Savart relation in the CVE method. By using the CVE method, we investigate the role of the coherent vorticity in the enstrophy transport near the T/NT interface by analyzing the coherent and incoherent contributions to the enstrophy transport equation. In Sec. II, the DNS of the planar jet is described. The procedure of the T/NT interface detection and the CVE method are described in Secs. III and IV, respectively. The numerical results are presented in Sec. V. Finally, the conclusions are summarized in Sec. VI.

II. DIRECT NUMERICAL SIMULATION OF A PLANAR JET

A. Numerical methods and computational parameters

The CVE method is applied to the DNS result of a spatially developing planar jet.[28] The numerical methods and simulation conditions are described here. In this work, the incompressible planar jet illustrated in Fig. 1 is considered. The origin of the coordinate system is located at the center of the jet inlet. The streamwise, lateral, and spanwise directions are represented by x, y, and z, respectively. The governing equations are the continuity equation and Navier–Stokes equations, which are written as follows:

$$\frac{\partial U_j}{\partial x_j} = 0, \tag{1}$$

$$\frac{\partial U_i}{\partial t} + \frac{\partial U_j U_i}{\partial x_j} = -\frac{1}{\rho}\frac{\partial p}{\partial x_i} + \nu \frac{\partial^2 U_i}{\partial x_j \partial x_j}, \tag{2}$$

where U_i is the instantaneous velocity component, ρ is the density, p is the instantaneous pressure, and ν is the kinematic viscosity.

The governing equations are solved using a finite difference method. The fully conservative fourth-order central difference proposed by Morinishi *et al.*[29] is used for spatial discretization in the x and z directions, and the fully conservative second-order central difference[29] is used for spatial discretization in the y direction. The continuity equation and Navier–Stokes equations are solved using the fractional step method. The Poisson equation is solved by the fast Fourier transform (in the spanwise direction), the cosine transform (in the streamwise direction), and a tridiagonal matrix algorithm (in the cross-streamwise direction). The Crank–Nicolson method is used for the time integration of the y-direction viscous term, and the third-order Runge–Kutta method is used for the time integration of the other terms. The extent of the computational domain is $(L_x, L_y, L_z) = (9.0\pi d, 7.3\pi d, 1.2\pi d)$, and $N_x \times N_y \times N_z = 2,048 \times 600 \times 128$ computational grid points are used in the DNS. The grid is equidistant in the x and z directions, whereas the non-equidistant grid is used in the y direction. In the y direction, a fine grid is used near the jet centerline, and the grid is stretched near the lateral boundaries. The Reynolds number based on the width of the jet inlet d and the mean bulk velocity at the jet inlet U_{J} is $Re = U_{\mathrm{J}} d/\nu = 2,200$. The convective boundary condition[30] is applied to the y–z plane at $x = L_x$. At the lateral boundaries, the y-directional gradient of velocity is set to zero, and the periodic boundary condition is applied in the spanwise direction. At $x = 0$ in the ambient flow, the cross-streamwise and spanwise velocities are set to zero without any fluctuations. The streamwise velocity of the ambient flow at $x = 0$ is $U_{\mathrm{A}} = 0.056 U_{\mathrm{J}}$. The measured

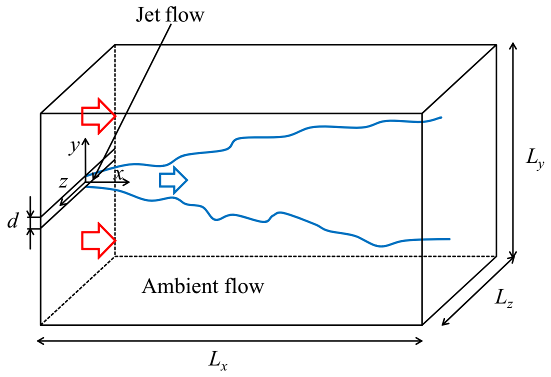

FIG. 1. Computational domain of a planar jet.

TABLE I. Coefficients in Eqs. (3)–(6) used to determine boundary condition at jet inlet.

n	0	1	2	3	4	5
A_n	1.303×10^{0}	-9.236×10^{-1}	-8.571×10^{0}	-1.207×10^{2}	3.464×10^{2}	0
$B_{u,n}$	4.673×10^{-2}	5.470×10^{-2}	-1.368×10^{0}	1.043×10^{1}	-1.657×10^{1}	0
$B_{v,n}$	3.505×10^{-2}	-1.558×10^{-2}	5.192×10^{-1}	-1.249×10^{0}	0	0
$B_{w,n}$	3.505×10^{-2}	-3.551×10^{-3}	1.930×10^{-1}	-1.186×10^{0}	7.355×10^{0}	-1.267×10^{1}

streamwise velocity statistics at the jet inlet[31–33] are used to determine the inflow velocity at the jet inlet. The inflow velocity is generated by a diffusion process that converts the random noise into the fluctuations which possess the required length scales.[34] According to Stanley *et al.*,[35] the length scale which corresponds to the fundamental mode for the shear layer near the jet inlet is used as the integral length scales of the velocity fluctuations at the jet inlet, which are set to $0.29d$ in the present DNS. The inflow velocity at the jet inlet is generated so that the lateral profiles of the streamwise mean velocity (U_{in}) and the rms values of the velocity fluctuations (u_{rms}, v_{rms}, w_{rms}) at the jet inlet satisfy the following equations:

$$\frac{U_{\mathrm{in}}(y) - U_{\mathrm{A}}}{U_{\mathrm{J}}} = \sum_{n=0}^{5} A_n \left(\frac{y}{d}\right)^{2n}, \tag{3}$$

$$\frac{u_{\mathrm{rms}}(y)}{U_{\mathrm{J}}} = \frac{1}{20} \sum_{n=0}^{5} B_{u,n} \left|\frac{y}{d}\right|^{n}, \tag{4}$$

$$\frac{v_{\mathrm{rms}}(y)}{U_{\mathrm{J}}} = \frac{1}{20} \sum_{n=0}^{5} B_{v,n} \left|\frac{y}{d}\right|^{n}, \tag{5}$$

$$\frac{w_{\mathrm{rms}}(y)}{U_{\mathrm{J}}} = \frac{1}{20} \sum_{n=0}^{5} B_{w,n} \left|\frac{y}{d}\right|^{n}. \tag{6}$$

The coefficients A_n, $B_{u,n}$, $B_{v,n}$, and $B_{w,n}$, are summarized in Table I. The mean cross-streamwise and spanwise velocities are zero at the jet inlet. In Fig. 2, the measurement results in the experimental apparatus[31–33] for $U_{\mathrm{in}}(y)$ and $u_{\mathrm{rms}}(y)$ are compared with Eqs. (3) and (4). Equations (3)–(6) are used to generate the inflow velocity. Although the mean velocity profile is similar to that in the experiments,[31–33] the measured rms value $u_{\mathrm{rms}}(y)$ is 20 times larger than Eq. (4). The small rms velocity is used for the boundary condition at the jet inlet. For the jet development, velocity fluctuations at large scales are important because small-scale fluctuations decay near the jet inlet.

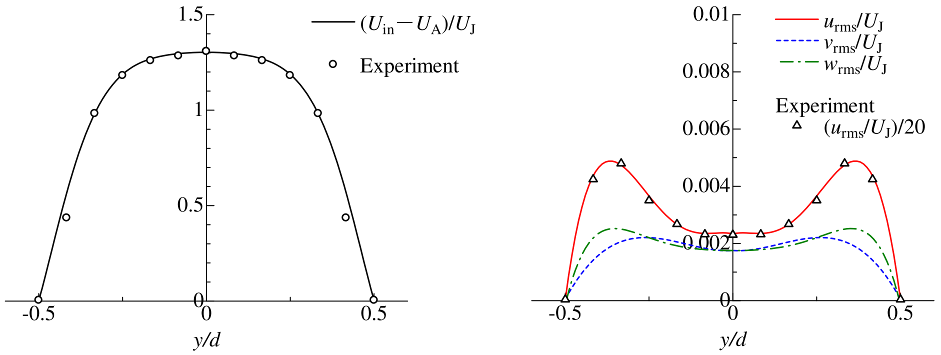

(a) Mean streamwise velocity

(b) Rms values of velocity fluctuations

FIG. 2. (a) Mean streamwise velocity and (b) rms values of the velocity fluctuations at jet inlet. Lateral profiles of velocity statistics at jet inlet are compared with measurement results.[31–33]

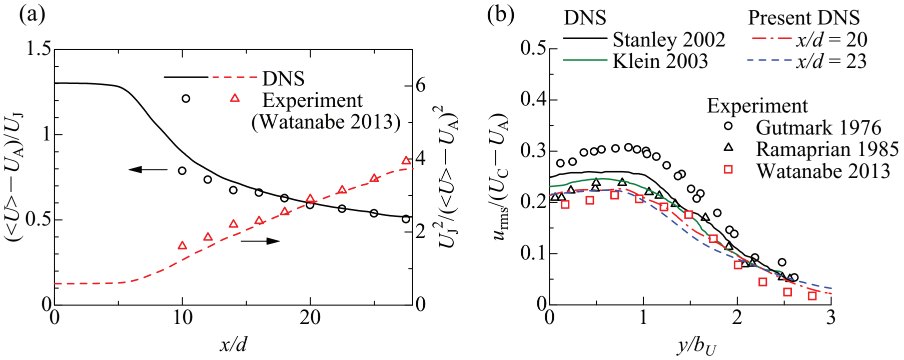

FIG. 3. Comparison of streamwise velocity statistics between the DNS results and the experimental results. (a) Streamwise evolution of the mean streamwise velocity on the jet centerline. (b) Lateral profiles of the rms value of the streamwise velocity fluctuation. The experiments by Gutmark and Wygnansk,[36] Ramaprian and Chandrasekhara,[37] and Watanabe *et al.*[31–33] and the DNSs by Stanley *et al.*[35] and Klein *et al.*[38] are compared with the present DNS results.

The velocity fluctuations generated by the diffusion process contain most of energy at large scales. Although the total energy represented by rms values is small, the generated velocity fluctuations contain energy at large enough scales to develop the jet flow.

B. Validations of the DNS results

The time-averaged statistics obtained by the present DNS are compared with those obtained by the experiments and the previous DNSs. Figure 3(a) shows the mean streamwise velocity $\langle U \rangle$ on the jet centerline. Here, $\langle\ \rangle$ denotes the time-averaged value. The present DNS result shows good agreement with the experimental result. The mean streamwise velocity on the jet centerline is also found to evolve according to $(\langle U \rangle - U_A) \propto (x/d)^{-1/2}$. Figure 3(b) shows the lateral profiles of the rms value of the streamwise velocity fluctuation $(u_{rms}/U_C - U_A)$. Here, U_C is the mean streamwise velocity on the jet centerline. The jet half-width based on $(\langle U \rangle - U_A)$, denoted by b_U, is used to normalize the lateral coordinate y. Self-similar profiles of $u_{rms}/U_C - U_A$ can be observed in the present DNS results. The lateral profiles of $u_{rms}/U_C - U_A$ in the present DNS are similar to those in the experiments and the previous DNSs. Thus, typical properties of the planar jet can be observed in the present DNS results.

We investigate the T/NT interface detected in the region of $22.5 \leq x/d \leq 23.5$, which is in the self-similar region. Reynolds number based on the Taylor microscale is $Re_\lambda = u_{rms}\lambda_x/\nu = 84$ at $x/d = 23$ on the jet centerline. Here, $\lambda_i = \sqrt{\langle u_i'^2 \rangle / \langle (\partial u_i'/\partial x_i)^2 \rangle}$ is the i-direction Taylor microscale, and $u_i' = U_i - \langle U_i \rangle$ is the velocity fluctuation. The computational grid size is about 1.2η at $x/d = 23$, where $\eta = (\nu^3/\epsilon)^{1/4}$ (ϵ: dissipation of turbulent kinetic energy) is the Kolmogorov lengthscale. The spatial resolution of the present DNS is small compared with the previous DNS studies on a spatially developing jet at similar Reynolds numbers.[35,38]

III. T/NT INTERFACE IN A PLANAR JET

A. Detection of the T/NT interface

According to the previous studies,[11,39] the vorticity magnitude $|\boldsymbol{\omega}|$ normalized by b_U and U_C is used to detect the T/NT interface. The flow region where the normalized vorticity magnitude $|\boldsymbol{\omega}|b_U/U_C$ is larger than a certain threshold ω_{th} is defined as the turbulent region. Therefore, the T/NT interface is defined as the isosurface of $|\boldsymbol{\omega}|b_U/U_C = \omega_{th}$. The threshold ω_{th} is determined according to the procedure used by Taveira *et al.*[11] First, we calculate the volume fraction of the turbulent region $\mathrm{Vol_T}$ as a function of ω_{th}. The volume of the turbulent region can be calculated as the volume of the region of $|\boldsymbol{\omega}|b_U/U_C \geq \omega_{th}$. Because we investigate the T/NT interface around

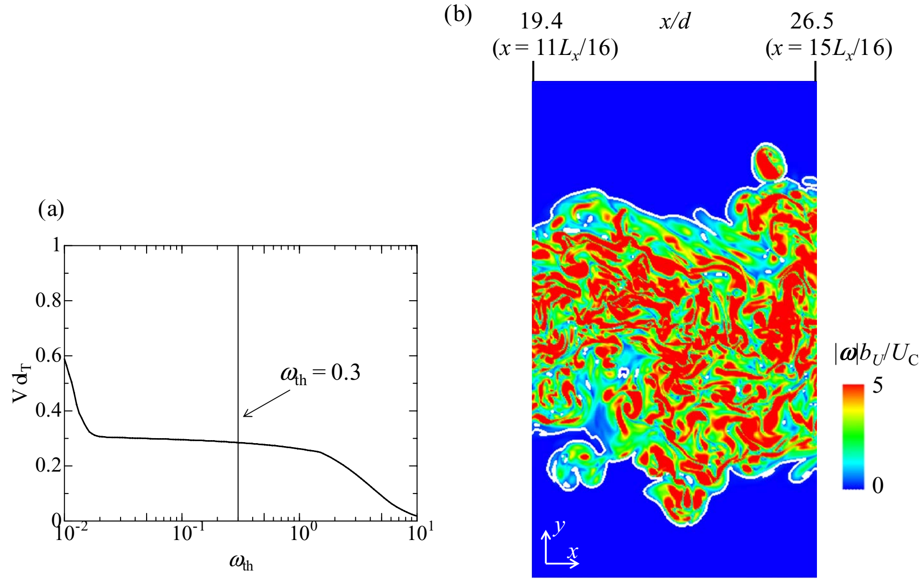

FIG. 4. Detection of the T/NT interface by thresholding vorticity magnitude. (a) The volume fraction of the turbulent region in the region of $11L_x/16 \leq x \leq 15L_x/16$, $-L_y/2 \leq y \leq L_y/2$, and $-L_z/2 \leq z \leq L_z/2$ as a function of the threshold ω_{th}. (b) Visualization of the T/NT interface and the vorticity field on a x–y plane for the interface detection threshold $\omega_{\mathrm{th}} = 0.3$. White lines represent the T/NT interface (isosurface of $|\boldsymbol{\omega}|b_U/U_C = 0.3$). Color contours represent the normalized vorticity magnitude $|\boldsymbol{\omega}|b_U/U_C$. Blue: $|\boldsymbol{\omega}|b_U/U_C = 0$, red: $|\boldsymbol{\omega}|b_U/U_C \geq 5$.

$x/d = 23$, $\mathrm{Vol}_{\mathrm{T}}$ is calculated in the region of $11L_x/16 \leq x \leq 15L_x/16$, whose volume is represented $L_x/4 \times L_y \times L_z$. $N_x/4 \times N_y \times N_z$ computational grid points are involved in this region. Figure 4(a) shows the relationship between $\mathrm{Vol}_{\mathrm{T}}$ and ω_{th}. As the threshold ω_{th} becomes large, the turbulent volume decreases. However, there is a plateau of the turbulent volume for a wide range of ω_{th}. Taveira *et al.*[11] showed that the T/NT interface location is almost independent of the interface detection threshold when the threshold is selected from the plateau like region in Fig. 4(a). We use $\omega_{\mathrm{th}} = 0.3$ as the interface detection threshold.

Figure 4(b) shows a snapshot of the vorticity field and the detected T/NT interface on a x–y plane. In Fig. 4(b), the isosurface of $|\boldsymbol{\omega}|b_U/U_C = 0.3$ which represents the T/NT interface is shown by white lines. The T/NT interface is convoluted and envelops the high vorticity region.

B. Conditional statistics conditioned on the distance from the T/NT interface

The conditional statistics conditioned on the distance from the T/NT interface are calculated using a procedure similar to that in previous works.[39,40] Figure 5 shows a schematic of T/NT interface in a jet flow. The local coordinate y_{I} and the interface height Y_{I} are defined as shown in Fig. 5. The

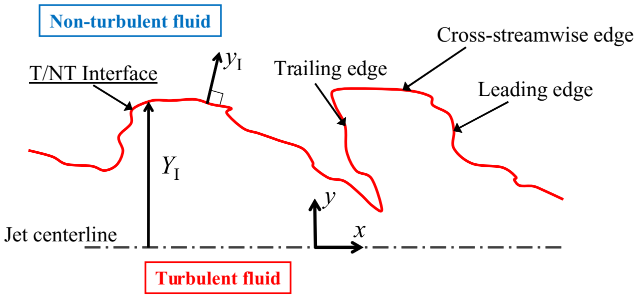

FIG. 5. Schematic of T/NT interface in a jet flow and definition of interface orientation.

location of the T/NT interface is represented by $y_{\mathrm{I}} = 0$. Here, y_{I} is taken to be normal to the T/NT interface. The turbulent fluid is on the side of negative y_{I}, whereas the non-turbulent fluid is on the side of positive y_{I}. We use $\langle\ \rangle_{\mathrm{I}}$ to represent the conditional average conditioned on y_{I}. We consider three orientations of the T/NT interface, which are called the cross-streamwise edge, leading edge, and trailing edge. These interface orientations are distinguished by the unit vector normal to the T/NT interface, $\mathbf{n} = -\nabla\omega^2/|\nabla\omega^2|$. At the cross-streamwise edge, $\mathbf{n}$ is parallel to the y direction. At the leading and trailing edges, $\mathbf{n}$ is parallel to the x direction, and the leading and trailing edges face the x and $-x$ directions, respectively. The conditional statistics conditioned on y_{I} are calculated for each interface orientation. In this calculation, deviations of the interface orientation within ±25° are accepted. This criterion for the interface orientation is the same as that in Bisset *et al.*[39] For example, the interface at which the angle between $\mathbf{n}$ and the cross-streamwise direction is smaller than 25° is used as the cross-streamwise edge for calculating the conditional statistics. For the interface detected as the cross-streamwise edge, y_{I} is set to be parallel to the cross-streamwise direction, although the angle between $\mathbf{n}$ and the cross-streamwise direction might not be zero. Similarly, for the interfaces detected as the leading and trailing edges, y_{I} is set to be parallel to the streamwise direction.

The conditional statistics are calculated for the turbulent and non-turbulent sides of the T/NT interface. When the conditional statistics are calculated for a T/NT interface, other interfaces can appear near the T/NT interface. The characteristics of the flow field drastically vary near the T/NT interface, and the width of this variation is of the order of the Taylor microscale. Therefore, when other interfaces appear near the T/NT interface, the region within λ away from the other interfaces is not used for calculating the conditional statistics, where λ is the Taylor microscale $\lambda = (\lambda_x + \lambda_y + \lambda_z)/3$ on the jet centerline. The existence of other interfaces is examined only in the direction of y_{I}. As shown in Fig. 4(b), "holes" of non-turbulent fluids are detected in the turbulent region when $\omega_{\mathrm{th}} = 0.3$ is used as the threshold. These holes of non-turbulent fluids are not used for calculating the conditional statistics.

IV. COHERENT VORTICITY EXTRACTION IN A PLANAR JET

A. Coherent vorticity extraction based on an orthogonal wavelet decomposition

The wavelet-based CVE method used in this work is described here. The CVE method proposed by Farge *et al.*[15,16] is based on the wavelet decomposition of vorticity. We consider the vorticity field $\boldsymbol{\omega}(x, y, z) = (\omega_x, \omega_y, \omega_z)$ and the computational domain represented by $(N_x^W \times N_y^W \times N_z^W) = (2^{J_x} \times 2^{J_y} \times 2^{J_z})$ grid points. First, the three-dimensional wavelet transform is applied to the vorticity components in the x, y, and z directions. Then, the vorticity components are represented in wavelet space by using the chosen wavelets and the wavelet coefficients $\tilde{\boldsymbol{\omega}} = (\tilde{\omega}_x, \tilde{\omega}_y, \tilde{\omega}_z)$, which contain information on scales, positions, and directions. In the CVE method, the coherent and incoherent vorticities are obtained by the inverse wavelet transform of the wavelet coefficients for the coherent and incoherent parts, which are obtained by thresholding the wavelet coefficients. The CVE algorithm is summarized below.

1. The wavelet coefficients $\tilde{\boldsymbol{\omega}} = (\tilde{\omega}_x, \tilde{\omega}_y, \tilde{\omega}_z)$ are computed from the vorticity field $\boldsymbol{\omega} = (\omega_x, \omega_y, \omega_z)$ by using the fast wavelet transform.
2. The first threshold ϵ_{th} is calculated from

$$\epsilon_{\mathrm{th}} = \sqrt{\frac{2\langle\boldsymbol{\omega}\cdot\boldsymbol{\omega}\rangle_f}{3}\ln N}. \tag{7}$$

   Here, $N = N_x^W \times N_y^W \times N_z^W$ is the number of the computational grid points, and $\langle\ \rangle_f$ denotes the spatial average in the computational domain in one realization of the flow.
3. The wavelet coefficients $\tilde{\boldsymbol{\omega}}$ are decomposed into the coherent ($\tilde{\boldsymbol{\omega}}^C$) and incoherent ($\tilde{\boldsymbol{\omega}}^I$) parts by thresholding $|\tilde{\boldsymbol{\omega}}|$

$$\tilde{\boldsymbol{\omega}}^C = \begin{cases} \tilde{\boldsymbol{\omega}} & \text{for } |\tilde{\boldsymbol{\omega}}| > \epsilon_{\mathrm{th}} \\ 0 & \text{otherwise} \end{cases}, \qquad \tilde{\boldsymbol{\omega}}^I = \begin{cases} \tilde{\boldsymbol{\omega}} & \text{for } |\tilde{\boldsymbol{\omega}}| \le \epsilon_{\mathrm{th}} \\ 0 & \text{otherwise} \end{cases}. \tag{8}$$

4. The new threshold is determined from Eq. (7) by using the incoherent vorticity. The threshold can be directly calculated in wavelet space using Parseval's relation. The wavelet coefficients are decomposed into $\tilde{\boldsymbol{\omega}}^C$ and $\tilde{\boldsymbol{\omega}}^I$ by using the new threshold and Eq. (8). This procedure iterates until the number of $\tilde{\boldsymbol{\omega}}^I$ does not change by the iteration.
5. The inverse fast wavelet transform is applied to $\tilde{\boldsymbol{\omega}}^C$ for reconstructing the coherent vorticity $\boldsymbol{\omega}^C$. Similarly, the incoherent vorticity $\boldsymbol{\omega}^I$ is reconstructed by the inverse fast wavelet transform of $\tilde{\boldsymbol{\omega}}^I$. Thus, we can decompose the vorticity

$$\boldsymbol{\omega} = \boldsymbol{\omega}^C + \boldsymbol{\omega}^I. \tag{9}$$

6. The coherent and incoherent velocity fields are reconstructed from the coherent and incoherent vorticities by using the Biot–Savart relation $\mathbf{U} = -\nabla \times (\nabla^{-2}\boldsymbol{\omega})$, respectively. Thus, the velocity field $\mathbf{U}$ is decomposed into

$$\mathbf{U} = \mathbf{U}^C + \mathbf{U}^I. \tag{10}$$

The threshold ϵ_{th} is chosen as the optimal value for denoising signals.[41] The iteration method (step 4) to determine the threshold was proposed by Azzalini *et al.*[42] Similar to the previous study,[20] we perform one iteration in the iterative procedure instead of the full iteration because of the fast convergence of the iterative procedure.[17] The wavelet transform used in this study assumes that the computational domain is periodic. However, the flow field analyzed by the CVE method is not periodic in the x and y directions. This difference may affect the extracted coherent field near the boundaries which face in the x and y directions. Therefore, we investigate statistics around $x/d = 23$, which is far away from the x-direction boundaries. It should be noted that the y-direction boundaries are also located far away from the jet.

B. Coherent vorticity extraction in a planar jet

The CVE method is applied to the planar jet. The Coiflet 12[43] is used as the wavelet in the CVE method. We also applied the CVE method using the Coiflet 6, and it was confirmed that both wavelets yield similar results. The coherent vorticity is extracted in the region of $11L_x/16 \leq x \leq 15L_x/16$, whose volume is $L_x/4 \times L_y \times L_z$. This computational domain is represented by the $(N_x/4 \times N_y \times N_z) = (512 \times 600 \times 128)$ computational grid points. The non-equidistant grid is used in the y direction. Before applying the fast wavelet transform, the vorticity field $\boldsymbol{\omega}$ is interpolated onto a fine equidistant grid which is represented by $(N_x^W \times N_y^W \times N_z^W) = (512 \times 1024 \times 128)$ grid points. The linear interpolation in the y direction is used here. The CVE method is applied to $\boldsymbol{\omega}$ on the equidistant grid. The coherent and incoherent vorticities obtained on the equidistant grid are reinterpolated onto the non-equidistant grid which is used in the DNS. Finally, the coherent ($\mathbf{U}^C$) and incoherent ($\mathbf{U}^I$) velocities are computed by using the Biot–Savart relation on the non-equidistant grid. In our analysis, the time-average of ϵ_{th} is $2.75U_{\text{J}}/d$.

V. RESULTS AND DISCUSSIONS

A. Coherent vorticity in the planar jet

We compare the vorticity field among the total, coherent, and incoherent vorticities by visualizing the vorticities. Figures 6(a)–6(c) show the three-dimensional visualizations of the total, coherent, and incoherent vorticities, respectively. From Figs. 6(a) and 6(b), it can be seen that the coherent vorticity shows good agreement with the total vorticity, and the vorticity field is well represented by the coherent vorticity. The incoherent vorticity field is noise-like and structureless, and has weak amplitude as shown in Fig. 6(c). The coherent vorticity is similar to the total vorticity even near the x-direction boundaries. Thus, the nonperiodic computational domain has small influence on the coherent vorticity. Based on the time-averaged results, the coherent field is represented by using only $\langle N_C^W/N^W \rangle = 0.5$ % of the wavelet coefficients, where N_C^W is the number of the coherent coefficients in one realization of the flow and N^W is the total number of the wavelet coefficients,

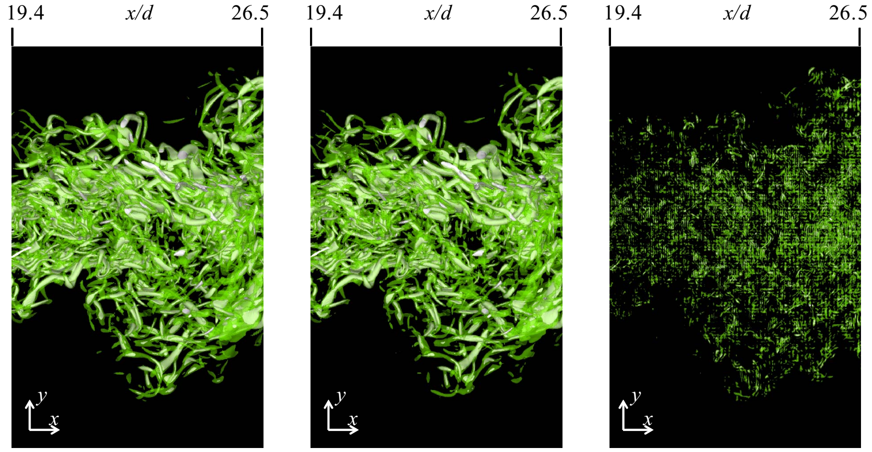

(a) Total vorticity (b) Coherent vorticity (c) Incoherent vorticity

FIG. 6. Three-dimensional visualization of the vorticity fields in the region of $11L_x/16 \leq x \leq 15L_x/16$. Here, $11L_x/16 = 19.4d$ and $15L_x/16 = 26.5d$. The vorticities are visualized by the isosurfaces of enstrophy. (a) Total vorticity. Green: $(\boldsymbol{\omega} \cdot \boldsymbol{\omega})/2 = 50(U_C/b_U)^2$. White: $(\boldsymbol{\omega} \cdot \boldsymbol{\omega})/2 = 100(U_C/b_U)^2$. (b) Coherent vorticity. Green: $(\boldsymbol{\omega}^C \cdot \boldsymbol{\omega}^C)/2 = 50(U_C/b_U)^2$. White: $(\boldsymbol{\omega}^C \cdot \boldsymbol{\omega}^C)/2 = 100(U_C/b_U)^2$. (c) Incoherent vorticity. Green: $(\boldsymbol{\omega}^I \cdot \boldsymbol{\omega}^I)/2 = 1.5(U_C/b_U)^2$. White: $(\boldsymbol{\omega}^I \cdot \boldsymbol{\omega}^I)/2 = 3(U_C/b_U)^2$.

which is determined by the computational grid used in the CVE. The mean enstrophy of the coherent vorticity is $\langle(\boldsymbol{\omega}^C \cdot \boldsymbol{\omega}^C)/2\rangle = 0.985\langle(\boldsymbol{\omega} \cdot \boldsymbol{\omega})/2\rangle$ at $(x, y) = (23d, 0)$, where $\langle(\boldsymbol{\omega} \cdot \boldsymbol{\omega})/2\rangle$ is the mean enstrophy of the total vorticity. For the enstrophy, the time-averaged values are also averaged in the spanwise (z) direction. Thus, the coherent vorticity contains 98.5% of the total enstrophy at $(x, y) = (23d, 0)$ on average. In contrast, $\langle N_I^W/N^W\rangle = 99.5\%$ of the wavelet coefficients are used to reconstruct the incoherent field, where N_I^W is the number of the incoherent coefficients in one realization of the flow. However, the mean enstrophy of the incoherent vorticity is $\langle(\boldsymbol{\omega}^I \cdot \boldsymbol{\omega}^I)/2\rangle = 0.015\langle(\boldsymbol{\omega} \cdot \boldsymbol{\omega})/2\rangle$ at $(x, y) = (23d, 0)$, and the incoherent vorticity contains only 1.5% of the total enstrophy on average. In the DNS, $N_x/4 \times N_y \times N_z = 512 \times 600 \times 128$ computational grid points are used for representing the computational domain analyzed by the CVE. The number of the coherent coefficients is 0.8% of the number of the computational grid points used in the DNS.

Figure 7(a) shows the probability density function (PDF) of the spanwise vorticity in the total (ω_z), coherent (ω_z^C), and incoherent (ω_z^I) fields obtained at $(x, y) = (23d, 0)$. In Fig. 7(a), the Gaussian profiles with the variance of ω_z^C and ω_z^I are shown by black solid lines. The PDF of ω_z^C agrees well with the PDF of the total vorticity, and shows the non-Gaussian profile. In contrast, the PDF of ω_z^I

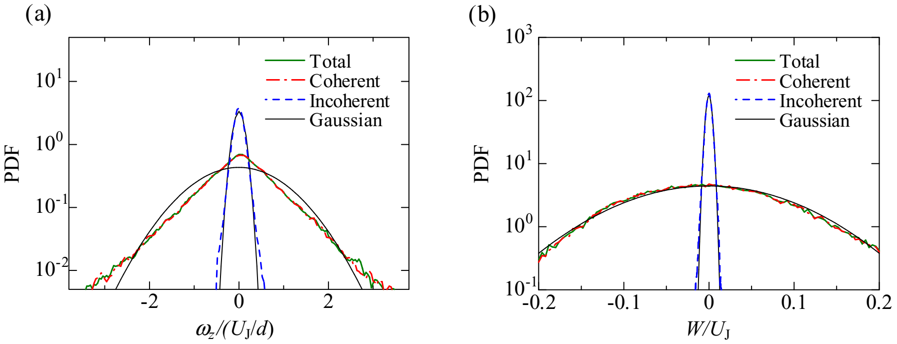

FIG. 7. PDF of (a) spanwise vorticity and (b) spanwise velocity in the total, coherent, and incoherent fields at $(x, y) = (23d, 0)$. The Gaussian profiles with the variance of spanwise vorticity and velocity in the coherent and incoherent fields are shown by black solid lines.

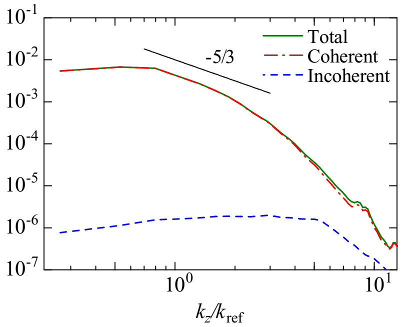

FIG. 8. Spatial one-dimensional spectrum (spanwise) of lateral velocity at $(x, y) = (23d, 0)$. The wavenumber k_z is normalized by the reference wavenumber $k_{\mathrm{ref}} = 2\pi/d$.

is similar to the Gaussian profile, and the variance of ω_z^I is small compared with that of the total vorticity. However, similar to the incoherent vorticity in the homogeneous isotropic turbulence,[18] the tail of the pdf shows a small difference from the Gaussian profile. Figure 7(b) compares the PDF of spanwise velocity W among the total, coherent, and incoherent fields. Both of the coherent and incoherent velocities have a PDF close to the Gaussian profile. The PDF of the coherent velocity is close to that in the total field, and the coherent velocity has a larger amplitude than incoherent one, in agreement with the previous study on the homogeneous isotropic turbulence.[18] Figure 8 shows the one-dimensional spectrum (spanwise direction) of lateral velocity. It is found that most of the energy of the velocity fluctuation is contained in the coherent field. The incoherent contribution becomes relatively important at a high-wavenumber range because the energy contained at the small scale in the total field is not as large as at the large scale. These results show that the CVE method successfully decomposes the vorticity in the jet into the coherent vorticity and the incoherent one.

B. Coherent vorticity near the T/NT interface

Figure 9 compares the T/NT interface represented by the total and coherent vorticities. The T/NT interface exhibits the convoluted structures. The interface for the coherent vorticity is not smooth. However, the large-scale geometry is very similar between the total and coherent vorticities. The viscous superlayer exists at the edge of the turbulent region while the turbulent sublayer appears between the turbulent core region and the viscous superlayer. The mean thickness of the viscous superlayer is about 5η,[3] and the intense vorticity structure does not exist in this region.[14] It can be considered that the viscous superlayer is more structureless than the turbulent sublayer. Therefore, a part of vorticity in the viscous superlayer might be discarded by the CVE, resulting in the nonsmooth T/NT interface for the coherent vorticity.

The conditional statistics conditioned on the distance from the T/NT interface are analyzed for investigating the coherent vorticity near the interface. The T/NT interface detected by using the total vorticity is used for calculating the conditional statistics for the total, coherent, and incoherent vorticities. Figure 10 shows the conditional average of the normalized vorticity magnitude $|\boldsymbol{\omega}|b_U/U_C$. In Fig. 10, the distance from the T/NT interface is normalized by the Taylor microscale $\lambda = (\lambda_x + \lambda_y + \lambda_z)/3$ on the jet centerline. The vorticity magnitude is small in the non-turbulent region. The conditional average of the vorticity magnitude shows a sharp jump near the T/NT interface. Within the distance λ, $\langle|\boldsymbol{\omega}|b_U/U_C\rangle_I$ almost reaches its value in the deep inside of the turbulent region. The width in the vorticity jump weakly depends on the interface orientation, and the width near the trailing edge is slightly larger than those near the cross-streamwise and leading edges. In contrast, magnitude of the normalized vorticity strongly depends on the interface orientation. The normalized vorticity magnitude is largest near the cross-streamwise edge, and smallest near the trailing edge among the three interface orientations.

The enstrophy $\omega^2/2 \equiv \omega_i\omega_i/2$ can be decomposed into the coherent and incoherent contributions using the CVE based on the orthogonal wavelet decomposition

$$\omega^2/2 = \omega_i^C\omega_i^C/2 + \omega_i^I\omega_i^I/2. \tag{11}$$

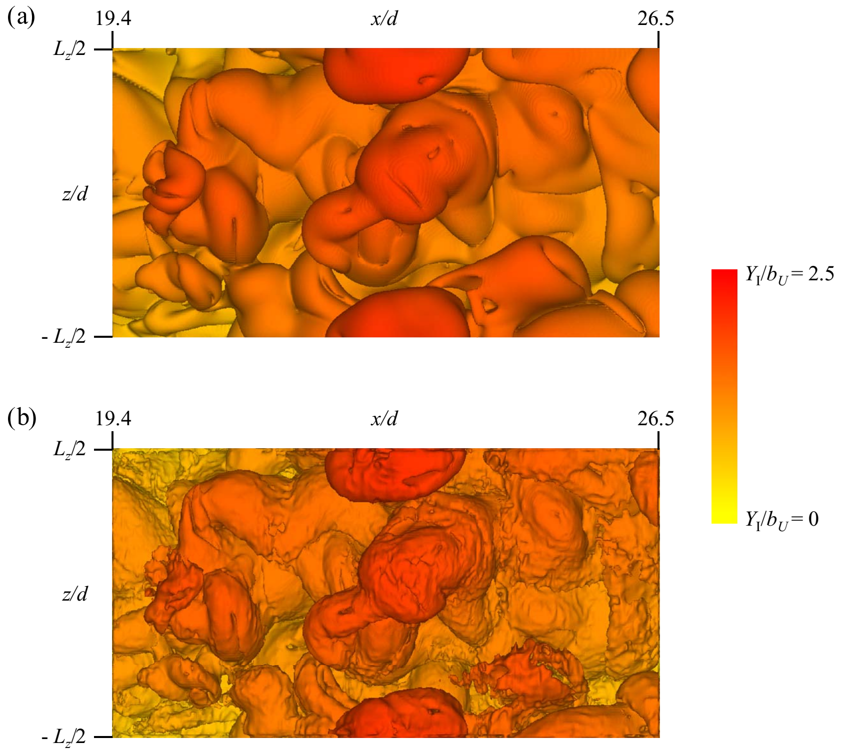

FIG. 9. The T/NT interface represented by (a) the total and (b) coherent vorticity detected in $y < 0$. The isosurface of the normalized vorticity magnitude ($|\boldsymbol{\omega}|b_U/U_\mathrm{C}$ and $|\boldsymbol{\omega}^C|b_U/U_\mathrm{C}$) is visualized. The color of the interface shows the normalized interface height Y_I/b_U.

Figure 11 shows the conditional average of the total enstrophy $\omega^2/2$, coherent enstrophy $\omega_i^C\omega_i^C/2$, and incoherent enstrophy $\omega_i^I\omega_i^I/2$. The enstrophy near the trailing edge is smallest among the three interface orientations. Most of the enstrophy is contained in the coherent vorticity in the deep inside of the turbulent region. The region near the T/NT interface is characterized by small enstrophy compared with the deep inside of the turbulent region. However, Fig. 11 shows that even near the T/NT interface, the coherent vorticity contains most of the enstrophy, and the incoherent contribution is small.

Figures 12(a) and 12(b) compare the streamwise (x), cross-streamwise (y), and spanwise (z) components of the vorticity vector between the total and coherent vorticities. The cross-streamwise vorticity, which is the normal component to the T/NT interface, is found to be the weakest component of the vorticity vector near the cross-streamwise edge. This tendency is related to the tangential

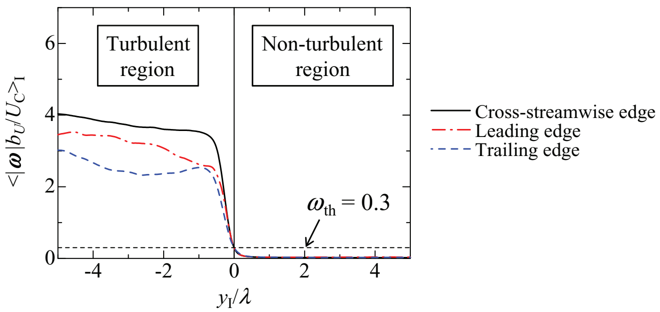

FIG. 10. Conditional average of the normalized vorticity magnitude near the cross-streamwise, leading, and trailing edges. The interface-detection threshold $\omega_\mathrm{th} = 0.3$ is shown by the black dashed line.

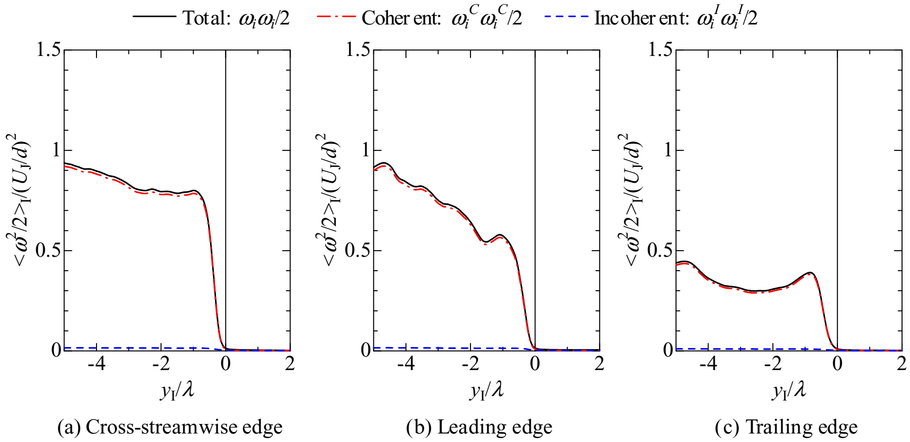

(a) Cross-streamwise edge (b) Leading edge (c) Trailing edge

FIG. 11. Coherent and incoherent contributions to enstrophy near the T/NT interface. (a) Cross-streamwise edge. (b) Leading edge. (c) Trailing edge.

alignment between the vorticity vector and the interface.[44] $\langle\omega_y^2\rangle_{\mathrm{I}}$ gradually increases toward the turbulent region near the cross-streamwise edge. In contrast, $\langle\omega_x^2\rangle_{\mathrm{I}}$ and $\langle\omega_z^2\rangle_{\mathrm{I}}$, which are the parallel components to the interface, show a sharp jump near the T/NT interface. $\langle\omega_z^2\rangle_{\mathrm{I}}$ has a large peak value slightly inside the T/NT interface. A comparison between Figs. 12(a) and 12(b) shows that these characteristics of the vorticity field near the T/NT interface are well captured by the coherent vorticity extracted by the CVE method.

C. Velocity field near the T/NT interface

The CVE decomposes the velocity field $\mathbf{U}$ into the coherent ($\mathbf{U}^C$) and incoherent ($\mathbf{U}^I$) velocities. Figure 13 shows the conditional average of the streamwise velocity U and the coherent (U^C) and incoherent (U^I) contributions to $\langle U\rangle_{\mathrm{I}}$. The results show that the incoherent contribution to the mean streamwise velocity is very small. The streamwise velocity in the turbulent region is faster than that in the non-turbulent region. However, the difference in $\langle U\rangle_{\mathrm{I}}$ between the turbulent and non-turbulent regions is small near the trailing edge. Near the cross-streamwise edge (Fig. 13(a)), the conditional average of U slightly inside the T/NT interface ($-1 \leq y_{\mathrm{I}}/\lambda \leq 0$) sharply increases toward the turbulent region, and then gradually increases toward the turbulent core region. Figure 14 shows the conditional average of the cross-streamwise velocity V and the coherent (V^C) and incoherent (V^I) contributions. Here, the cross-streamwise velocity toward the jet centerline is defined as negative.

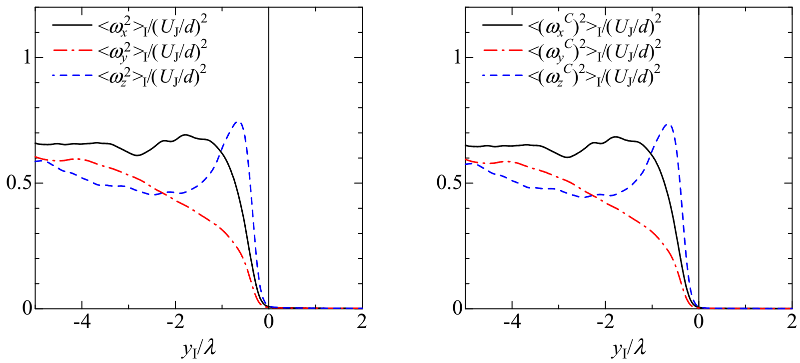

(a) Total vorticity (b) Coherent vorticity

FIG. 12. Comparison of streamwise (x), cross-streamwise (y), and spanwise (z) components of the vorticity vector between the total and coherent vorticities near the cross-streamwise edge. (a) Total vorticity. (b) Coherent vorticity.

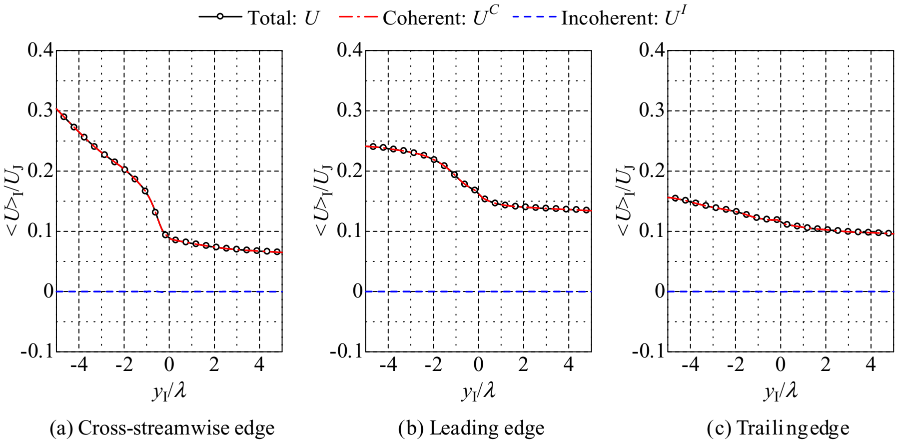

(a) Cross-streamwise edge (b) Leading edge (c) Trailing edge

FIG. 13. Conditional average of the streamwise velocity and the coherent and incoherent contributions to the streamwise velocity near the T/NT interface. (a) Cross-streamwise edge. (b) Leading edge. (c) Trailing edge.

The incoherent contribution to the mean cross-streamwise velocity is also very small. Near the cross-streamwise and leading edges, the conditional average of V is positive in the turbulent region away from the interface. This positive V in the turbulent region is expected to be caused by the jet expansion to the cross-streamwise direction. However, the cross-streamwise velocity near the trailing edge is negative even in the turbulent region. In the non-turbulent region near these interfaces, the conditional average of the cross-streamwise velocity is negative. This negative V in the non-turbulent region is caused by induced flows and large-scale engulfing motions.[12]

At $x = 0$, the streamwise velocity in the ambient flow is $U_A = 0.056U_J$. Figure 13(a) shows that the mean streamwise velocity in the non-turbulent region near the cross-streamwise edge is close to U_A. In contrast, the mean streamwise velocity in the non-turbulent region near the leading and trailing edges is larger than U_A. Figures 14(a)–14(c) show that the cross-streamwise velocity in the non-turbulent region near the leading and trailing edges is large in magnitude compared with that near the cross-streamwise edge. These conditional profiles of U and V in the non-turbulent region near the leading and trailing edges are related to the engulfing motion in the ambient flow. The non-turbulent fluid engulfed by the large-scale motion appears near the leading and trailing edges. The fluid in the non-turbulent region is drawn toward the turbulent core region by the large-scale motion. This large-scale engulfing motion is considered to cause large positive U and large negative V near the leading and trailing edges. Although the engulfing motion is not significant in

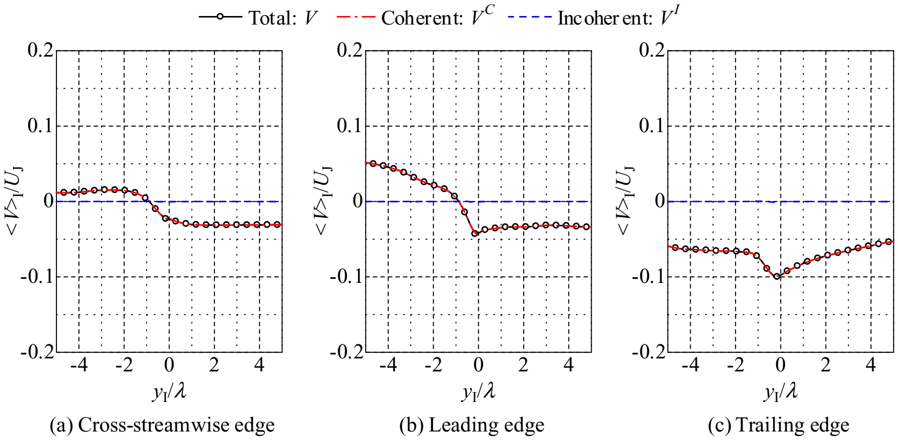

(a) Cross-streamwise edge (b) Leading edge (c) Trailing edge

FIG. 14. Conditional average of the cross-streamwise velocity and coherent and incoherent contributions to the cross-streamwise velocity near the T/NT interface. (a) Cross-streamwise edge. (b) Leading edge. (c) Trailing edge.

the local entrainment process at the interface,[11] it characterizes the flow field in the non-turbulent region, and contributes to the total entrainment process.[12] The small incoherent-contribution to the mean velocity indicates that the large-scale motion in the non-turbulent region is well represented by the coherent field, although the intense vorticity does not exist in this region as shown in Fig. 4(b). These results show that the large-scale motions in the non-turbulent region are not removed by extracting the coherent part of the flow field. An imprint of the large-scale motions appears in the mean velocity profile. If the mean flow does not exist as in shear-free turbulence,[45] there is no difference between the leading and trailing edges. Thus, the dependence of the flow field near the interface on the interface orientation is related to the large-scale motions or the mean flow field. This implies that the interface orientation effect can depend on the mean flow profile and the large-scale motions, which change depending on flow configurations.[12]

D. Enstrophy transport near the T/NT interface

We investigate the enstrophy transport by the coherent vorticity by analyzing the enstrophy transport equation, which is given by

$$\frac{\partial \omega^2/2}{\partial t} + \mathbf{U}\cdot\nabla(\omega^2/2) = \omega_i\omega_j S_{ij} + \nu\nabla^2(\omega^2/2) - \nu\nabla\omega_i\cdot\nabla\omega_i. \tag{12}$$

Here, $S_{ij} = (\partial U_i/\partial x_j + \partial U_j/\partial x_i)/2$ is the component of the rate of strain tensor. The first term on the right-hand side of Eq. (12) is the production term, the second term is the viscous diffusion term, and the third term is the viscous dissipation term.

The CVE decomposes the vorticity and velocity fields into the coherent and incoherent parts as shown in Eqs. (9) and (10), and we can extract the coherent contribution to the enstrophy transport. The enstrophy production term $P_\omega \equiv \omega_i\omega_j S_{ij}$ is decomposed into three terms

$$P_\omega = P_\omega^C + P_\omega^I + P_\omega^{CI}, \tag{13}$$

$$P_\omega^C \equiv \omega_i^C\omega_j^C S_{ij}^C, \tag{14}$$

$$P_\omega^I \equiv \omega_i^I\omega_j^I S_{ij}^I, \tag{15}$$

$$P_\omega^{CI} \equiv \omega_i^C\omega_j^I S_{ij}^C + \omega_i^I\omega_j^C S_{ij}^C + \omega_i^I\omega_j^I S_{ij}^C + \omega_i^C\omega_j^C S_{ij}^I + \omega_i^C\omega_j^I S_{ij}^I + \omega_i^I\omega_j^C S_{ij}^I. \tag{16}$$

Here, the rate of strain tensor is decomposed into $S_{ij} = S_{ij}^C + S_{ij}^I$, and $S_{ij}^C \equiv (\partial U_i^C/\partial x_j + \partial U_j^C/\partial x_i)/2$ and $S_{ij}^I \equiv (\partial U_i^I/\partial x_j + \partial U_j^I/\partial x_i)/2$ are the coherent and incoherent components of the rate of strain tensor, respectively. P_ω^C and P_ω^I are the enstrophy production by the coherent and incoherent vorticities, respectively. P_ω^{CI} consists of both coherent and incoherent components, and can be considered as the interaction between coherent and incoherent vorticities. The enstrophy diffusion term $D_\omega \equiv \nu\nabla^2(\omega^2/2)$ is decomposed into the coherent and incoherent contributions

$$D_\omega = D_\omega^C + D_\omega^I, \tag{17}$$

$$D_\omega^C \equiv \nu\nabla^2(\omega_i^C\omega_i^C/2), \tag{18}$$

$$D_\omega^I \equiv \nu\nabla^2(\omega_i^I\omega_i^I/2). \tag{19}$$

Thus, the diffusion term is simply represented by the coherent and incoherent contributions. The enstrophy dissipation term $\epsilon_\omega \equiv -\nu\nabla\omega_i\cdot\nabla\omega_i$ is decomposed into three terms

$$\epsilon_\omega = \epsilon_\omega^C + \epsilon_\omega^I + \epsilon_\omega^{CI}, \tag{20}$$

$$\epsilon_\omega^C \equiv -\nu\nabla\omega_i^C\cdot\nabla\omega_i^C, \tag{21}$$

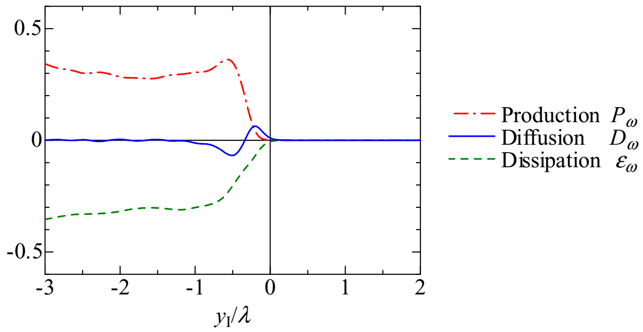

FIG. 15. Conditional average of the enstrophy production, diffusion, and dissipation terms in the total field near the cross-streamwise edge.

$$\epsilon_\omega^I \equiv -\nu \nabla \omega_i^I \cdot \nabla \omega_i^I, \tag{22}$$

$$\epsilon_\omega^{CI} \equiv -2\nu \nabla \omega_i^I \cdot \nabla \omega_i^C, \tag{23}$$

ϵ_ω^C and ϵ_ω^I are the viscous dissipation caused by the coherent and incoherent vorticities, respectively. The interaction between the coherent and incoherent vorticities (ϵ_ω^{CI}) also contributes to the enstrophy dissipation. These decompositions of the production, diffusion, and dissipation terms are used for investigating the coherent and incoherent contributions to the enstrophy transport near the T/NT interface.

Figure 15 shows the conditional average of the enstrophy production (P_ω), diffusion (D_ω), and dissipation (ϵ_ω) in the total field near the cross-streamwise edge. In the deep inside of the turbulent region ($y_\mathrm{I}/\lambda < -1$), the production almost balances the dissipation on average. This was also observed in a temporally developing jet.[11] The conditional average of the dissipation becomes small in magnitude from the deep inside of the turbulent region toward the T/NT interface. On the other hand, the conditional average of the production term has a peak value slightly inside the T/NT interface ($y_\mathrm{I}/\lambda \approx -0.6$). Thus, in this region, the enstrophy production exceeds the dissipation on average. The conditional average of the diffusion term has both positive and negative values near the T/NT interface, and the enstrophy in the turbulent region is transferred toward the T/NT interface. It should be noted that the enstrophy growth near the T/NT interface is caused by the viscous diffusion term. Therefore, the enstrophy diffusion by the viscous effect triggers the transition of the non-turbulent fluid to the turbulent one near the interface, resulting in the spread of turbulent regions.

Figure 16 shows the conditional average of the decomposed production, diffusion, and dissipation terms near the cross-streamwise edge. Figure 16(a) shows the enstrophy production by the total, coherent, and incoherent vorticities and the interaction between the coherent and incoherent vorticities. The production by the coherent vorticity P_ω^C is largest among P_ω^C, P_ω^I, and P_ω^{CI}, and the enstrophy production is mainly caused by the coherent vorticity. The enstrophy production by the incoherent vorticity P_ω^I is very small, and can be neglected. The conditional average of P_ω^{CI} is positive and has small non-zero values in the turbulent region. Therefore, the incoherent vorticity does not produce the enstrophy by itself, but can produce the enstrophy through its interaction with the coherent vorticity. The coherent vorticity accounts for $\langle P_\omega^C \rangle_\mathrm{I} / \langle P_\omega \rangle_\mathrm{I} = 90\%$ and 85% of the total enstrophy production at $y_\mathrm{I}/\lambda = -3.0$ (turbulent region away from the interface) and -0.3 (turbulent region near the interface), respectively. Figure 16(b) shows the viscous diffusion by the coherent (D_ω^C) and incoherent (D_ω^I) vorticities. The conditional average of D_ω^I is small, and can be neglected even near the T/NT interface. In contrast, the conditional profile of D_ω^C is similar to the profile of the total diffusion term D_ω. Therefore, the enstrophy diffusion is caused by the coherent vorticity. For the dissipation (Fig. 16(c)), the coherent vorticity has the largest contribution. However, the conditional averages of ϵ_ω^I and ϵ_ω^{CI} also have small non-zero values. The values of $\langle \epsilon_\omega^C \rangle_\mathrm{I} / \langle \epsilon_\omega \rangle_\mathrm{I}$ are 83% and 81% at $y_\mathrm{I}/\lambda = -3.0$ and -0.3, respectively. Thus, the enstrophy dissipation is caused by both coherent and incoherent vorticities, although the contributions of the incoherent vorticity and

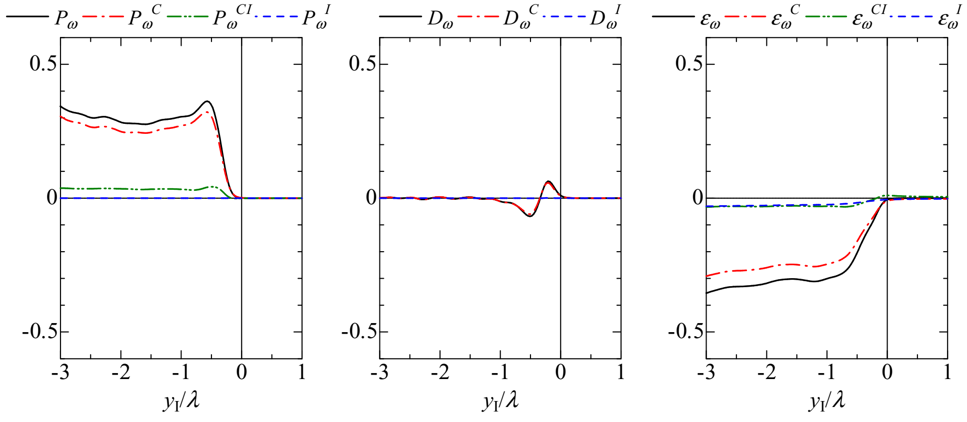

(a) Production (b) Diffusion (c) Dissipation

FIG. 16. Conditional average of the enstrophy (a) production, (b) diffusion, and (c) dissipation terms near the cross-streamwise edge. These terms are compared among the contributions of the coherent vorticity, the incoherent vorticity, and the interaction of the coherent and incoherent vorticities.

the interaction between the coherent and incoherent vorticities are small compared with that by the coherent vorticity.

The conditional profiles of the enstrophy transport equation decomposed by the CVE show that the coherent vorticity has large contributions to the enstrophy budget near the T/NT interface. The incoherent vorticity cannot be neglected in the enstrophy dissipation, and the interaction between the coherent and incoherent vorticities contributes both enstrophy production and dissipation. However, the enstrophy production and dissipation associated with the incoherent vorticity are small compared with the coherent contribution. The enstrophy diffusion near the T/NT interface is also caused by the coherent vorticity. The enstrophy growth in the non-turbulent region near the T/NT interface arises from the viscous diffusion, and causes the entrainment of non-turbulent fluids. The region near the interface where the viscous diffusion dominates the enstrophy growth can be related to the viscous superlayer, whose length scale is characterized by the Kolmogorov lengthscale.[3] The results show that the coherent vorticity well captures the small scale features near the T/NT interface, and is responsible to the local entrainment process, which is caused by the viscous effect near the interface. Thus, most of the enstrophy transport mechanism near the T/NT interface is well captured by the coherent vorticity extracted by the CVE method.

VI. CONCLUDING REMARKS

DNS of a planar jet was performed to investigate the vorticity field near the T/NT interface. The CVE method based on the orthogonal wavelet decomposition of vorticity was applied to the planar jet for extracting the coherent vorticity.

The coherent vorticity was reconstructed from small number of wavelet coefficients. Nevertheless, the coherent vorticity contains most of the enstrophy in the planar jet. Visualization of the total and coherent vorticities also shows that the vorticity field is well represented by the coherent vorticity. The large-scale convolutions of the interface can be seen in the visualization of the T/NT interface detected by the coherent vorticity.

The coherent vorticity near the T/NT interface is investigated by taking the conditional average conditioned on the distance from the interface. The coherent vorticity contains most of the enstrophy even near the T/NT interface, and the characteristics of the vorticity field near the interface are well captured by the coherent vorticity. The velocity fields corresponding to the coherent and incoherent vorticities were obtained by the Biot–Savart relation. The incoherent contribution to the mean velocity is very small near the T/NT interface, and the mean profile of the coherent velocity near the interface agrees well with the mean velocity profile of the total field. The non-turbulent fluids near the T/NT interface in a jet are characterized by the large-scale motions, such as induced flows and engulfing motions. These large-scale motions in the non-turbulent region are well represented by the coherent field, and they are not removed by extracting the coherent part of the flow field.

The coherent and incoherent contributions in the enstrophy transport are investigated by analyzing the enstrophy transport equation which is decomposed by the CVE. Although the incoherent vorticity and the interaction between the coherent and incoherent vorticities cannot be neglected in the enstrophy transport, the enstrophy production and dissipation associated with the incoherent vorticity are small compared with the coherent contribution. The enstrophy diffusion near the T/NT interface, which causes the local entrainment of non-turbulent fluids, arises from the coherent vorticity, and not by the incoherent vorticity. Thus, most of the enstrophy transport mechanism near the T/NT interface is well captured by the coherent vorticity extracted by the CVE method. Both large-scale motions (e.g., engulfment of non-turbulent fluids) and small-scale features (viscous diffusion of enstrophy) near the T/NT interface are well represented by the coherent vorticity extracted by the CVE method. These results motivate further development of the coherent vorticity simulation for free shear flows, which consist of both turbulent and non-turbulent flows.

ACKNOWLEDGMENTS

The authors would like to thank Dr. O. Terashima for his help in this study. The authors acknowledge Professor T. Ishihara, Dr. N. Okamoto (Nagoya University), Professor C. B. da Silva, and Mr. R. R. Taveira (Instituto Superior Técnico) for providing valuable comments. The authors also acknowledge the anonymous referees for valuable comments. Part of this work was conducted under the Collaborative Research Project of the Institute of Fluid Science, Tohoku University. This work was supported by JSPS KAKENHI Grant No. 25002531 and MEXT KAKENHI Grant Nos. 25289030, 25289031, and 25630052.

[1] C. B. da Silva, J. C. R. Hunt, I. Eames, and J. Westerweel, "Interfacial layers between regions of different turbulence intensity," Annu. Rev. Fluid Mech. **46**, 567 (2014).
[2] S. Corrsin and A. L. Kistler, "Free-stream boundaries of turbulent flows," NACA Technical Report No. TN-1244, 1955.
[3] R. R. Taveira and C. B. da Silva, "Characteristics of the viscous superlayer in shear free turbulence and in planar turbulent jets," Phys. Fluids **26**, 021702 (2014).
[4] J. Westerweel, T. Hofmann, C. Fukushima, and J. C. R. Hunt, "The turbulent/non-turbulent interface at the outer boundary of a self-similar turbulent jet," Exp. Fluids **33**, 873 (2002).
[5] J. Westerweel, C. Fukushima, J. M. Pedersen, and J. C. R. Hunt, "Mechanics of the turbulent-nonturbulent interface of a jet," Phys. Rev. Lett. **95**, 174501 (2005).
[6] J. Westerweel, C. Fukushima, J. M. Pedersen, and J. C. R. Hunt, "Momentum and scalar transport at the turbulent/non-turbulent interface of a jet," J. Fluid Mech. **631**, 199 (2009).
[7] M. Holzner, A. Liberzon, N. Nikitin, B. Lüthi, W. Kinzelbach, and A. Tsinober, "A Lagrangian investigation of the small-scale features of turbulent entrainment through particle tracking and direct numerical simulation," J. Fluid Mech. **598**, 465 (2008).
[8] M. Holzner, B. Lüthi, A. Tsinober, and W. Kinzelbach, "Acceleration, pressure and related quantities in the proximity of the turbulent/non-turbulent interface," J. Fluid Mech. **639**, 153 (2009).
[9] M. Holzner and B. Lüthi, "Laminar superlayer at the turbulence boundary," Phys. Rev. Lett. **106**, 134503 (2011).
[10] C. B. da Silva and J. C. F. Pereira, "The effect of subgrid-scale models on the vortices computed from large-eddy simulations," Phys. Fluids **16**, 4506 (2004).
[11] R. R. Taveira, J. S. Diogo, D. C. Lopes, and C. B. da Silva, "Lagrangian statistics across the turbulent-nonturbulent interface in a turbulent plane jet," Phys. Rev. E **88**, 043001 (2013).
[12] J. Philip and I. Marusic, "Large-scale eddies and their role in entrainment in turbulent jets and wakes," Phys. Fluids **24**, 055108 (2012).
[13] C. B. da Silva and R. R. Taveira, "The thickness of the turbulent/nonturbulent interface is equal to the radius of the large vorticity structures near the edge of the shear layer," Phys. Fluids **22**, 121702 (2010).
[14] C. B. da Silva, R. J. N. Dos Reis, and J. C. F. Pereira, "The intense vorticity structures near the turbulent/non-turbulent interface in a jet," J. Fluid Mech. **685**, 165 (2011).
[15] M. Farge, K. Schneider, and N. Kevlahan, "Non-Gaussianity and coherent vortex simulation for two-dimensional turbulence using an adaptive orthogonal wavelet basis," Phys. Fluids **11**, 2187 (1999).
[16] M. Farge, G. Pellegrino, and K. Schneider, "Coherent vortex extraction in 3D turbulent flows using orthogonal wavelets," Phys. Rev. Lett. **87**, 054501 (2001).
[17] K. Schneider and O. V. Vasilyev, "Wavelet methods in computational fluid dynamics," Annu. Rev. Fluid Mech. **42**, 473 (2010).
[18] M. Farge, K. Schneider, G. Pellegrino, A. A. Wray, and R. S. Rogallo, "Coherent vortex extraction in three-dimensional homogeneous turbulence: Comparison between CVS-wavelet and POD-Fourier decompositions," Phys. Fluids **15**, 2886 (2003).

[19] N. Okamoto, K. Yoshimatsu, K. Schneider, M. Farge, and Y. Kaneda, "Coherent vortices in high resolution direct numerical simulation of homogeneous isotropic turbulence: A wavelet viewpoint," Phys. Fluids **19**, 115109 (2007).

[20] M. Wilczek, B. Kadoch, K. Schneider, R. Friedrich, and M. Farge, "Conditional vorticity budget of coherent and incoherent flow contributions in fully developed homogeneous isotropic turbulence," Phys. Fluids **24**, 035108 (2012).

[21] T. Nabil, W. A. Kareem, S. Izawa, and Y. Fukunishi, "Extraction of coherent vortices from homogeneous turbulence using curvelets and total variation filtering methods," Comput. Fluids **57**, 76 (2012).

[22] W. A. Kareem, T. Nabil, S. Izawa, and Y. Fukunishi, "Harmonic analysis filtering techniques for forced and decaying homogeneous isotropic turbulence," Comput. Math. Appl. **65**, 1059 (2013).

[23] F. G. Jacobitz, L. Liechtenstein, K. Schneider, and M. Farge, "On the structure and dynamics of sheared and rotating turbulence: Direct numerical simulation and wavelet-based coherent vortex extraction," Phys. Fluids **20**, 045103 (2008).

[24] K. Schneider, M. Farge, G. Pellegrino, and M. Rogers, "CVS filtering of 3D turbulent mixing layers using orthogonal wavelets," *CTR Summer Program 2000* (NASA/Stanford University, Stanford, CA, 2000), pp. 319–330.

[25] K. Schneider, M. Farge, G. Pellegrino, and M. M. Rogers, "Coherent vortex simulation of three-dimensional turbulent mixing layers using orthogonal wavelets," J. Fluid Mech. **534**, 39 (2005).

[26] G. Khujadze, R. Nguyen van Yen, K. Schneider, M. Oberlack, and M. Farge, "Coherent vorticity extraction in turbulent boundary layers using orthogonal wavelets," J. Phys. Conf. Ser. **318**, 022011 (2011).

[27] O. Roussel and K. Schneider, "Coherent vortex simulation of weakly compressible turbulent mixing layers using adaptive multiresolution methods," J. Comput. Phys. **229**, 2267 (2010).

[28] T. Watanabe, Y. Sakai, K. Nagata, O. Terashima, H. Suzuki, T. Hayase, and Y. Ito, "Visualization of turbulent reactive jet by using direct numerical simulation," Int. J. Model. Simul. Sci. Comput. **04**, 1341001 (2013).

[29] Y. Morinishi, T. S. Lund, O. V. Vasilyev, and P. Moin, "Fully conservative higher order finite difference schemes for incompressible flow," J. Comput. Phys. **143**, 90 (1998).

[30] Y. Dai, T. Kobayashi, and N. Taniguchi, "Large eddy simulation of plane turbulent jet flow using a new outflow velocity boundary condition," JSME Int. J., Ser. B **37**, 242 (1994).

[31] T. Watanabe, Y. Sakai, K. Nagata, O. Terashima, and T. Kubo, "Simultaneous measurements of reactive scalar and velocity in a planar liquid jet with a second-order chemical reaction," Exp. Fluids **53**, 1369 (2012).

[32] T. Watanabe, Y. Sakai, K. Nagata, and O. Terashima, "Joint statistics between velocity and reactive scalar in a turbulent liquid jet with a chemical reaction," Phys. Scr. **T155**, 014039 (2013).

[33] T. Watanabe, Y. Sakai, K. Nagata, and O. Terashima, "Turbulent Schmidt number and eddy diffusivity change with a chemical reaction," J. Fluid Mech. **754**, 98 (2014).

[34] A. Kempf, M. Klein, and J. Janicka, "Efficient generation of initial-and inflow-conditions for transient turbulent flows in arbitrary geometries," Flow, Turbul. Combust. **74**, 67 (2005).

[35] S. A. Stanley, S. Sarkar, and J. P. Mellado, "A study of the flow-field evolution and mixing in a planar turbulent jet using direct numerical simulation," J. Fluid Mech. **450**, 377 (2002).

[36] E. Gutmark and I. Wygnansk, "The planar turbulent jet," J. Fluid Mech. **73**, 465 (1976).

[37] B. R. Ramaprian and M. S. Chandrasekhara, "LDA measurements in plane turbulent jets," Trans. ASME: J. Fluids Eng. **107**, 264 (1985).

[38] M. Klein, A. Sadiki, and J. Janicka, "Investigation of the influence of the Reynolds number on a plane jet using direct numerical simulation," Int. J. Heat Fluid Flow **24**, 785 (2003).

[39] D. K. Bisset, J. C. R. Hunt, and M. M. Rogers, "The turbulent/non-turbulent interface bounding a far wake," J. Fluid Mech. **451**, 383 (2002).

[40] C. B. da Silva and J. C. F. Pereira, "Invariants of the velocity-gradient, rate-of-strain, and rate-of-rotation tensors across the turbulent/nonturbulent interface in jets," Phys. Fluids **20**, 055101 (2008).

[41] D. L. Donoho and J. M. Johnstone, "Ideal spatial adaptation by wavelet shrinkage," Biometrika **81**, 425 (1994).

[42] A. Azzalini, M. Farge, and K. Schneider, "Nonlinear wavelet thresholding: A recursive method to determine the optimal denoising threshold," Appl. Comput. Harmon. Anal. **18**, 177 (2005).

[43] I. Daubechies, *Ten Lectures on Wavelets*, CBMS-NSF Regional Conference Series in Applied Mathematics Vol. **61** (SIAM, Philadelphia, 1992).

[44] C. B. da Silva and R. J. N. dos Reis, "The role of coherent vortices near the turbulent/non-turbulent interface in a planar jet," Philos. Trans. R. Soc. London, Ser. A **369**, 738 (2011).

[45] M. A. C. Teixeira and C. B. da Silva, "Turbulence dynamics near a turbulent/non-turbulent interface," J. Fluid Mech. **695**, 257 (2012).